

# Fast Joint Reconstruction of Dynamic $R_2^*$ and Field Maps in Functional MRI

Valur T. Olafsson\*, *Student Member, IEEE*, Douglas C. Noll, *Member, IEEE*, and Jeffrey A. Fessler, *Fellow, IEEE*

**Abstract**—Blood oxygen level dependent (BOLD) functional magnetic resonance imaging (fMRI) is conventionally done by reconstructing  $T_2^*$ -weighted images. However, since the images are unites they are nonquantifiable in terms of important physiological parameters. An alternative approach is to reconstruct  $R_2^*$  maps which are quantifiable and have comparable BOLD contrast as  $T_2^*$ -weighted images. However, conventional  $R_2^*$  mapping involves long readouts and ignores relaxation during readout. Another problem with fMRI imaging is temporal drift/fluctuations in off-resonance. Conventionally, a field map is collected at the start of the fMRI study to correct for off-resonance, ignoring any temporal changes. Here, we propose a new fast regularized iterative algorithm that jointly reconstructs  $R_2^*$  and field maps for all time frames in fMRI data. To accelerate the algorithm we linearize the MR signal model, enabling the use of fast regularized iterative reconstruction methods. The regularizer was designed to account for the different resolution properties of both  $R_2^*$  and field maps and provide uniform spatial resolution. For fMRI data with the same temporal frame rate as data collected for  $T_2^*$ -weighted imaging the resulting  $R_2^*$  maps performed comparably to  $T_2^*$ -weighted images in activation detection while also correcting for spatially global and local temporal changes in off-resonance.

**Index Terms**—Field map, functional magnetic resonance imaging (fMRI), joint reconstruction, linear approximation, magnetic field drift correction, physiological noise correction,  $R_2^*$ .

## I. INTRODUCTION

THE most common method of imaging brain activation in functional magnetic resonance imaging (fMRI) is through the blood oxygen level dependent (BOLD) contrast mechanism. This contrast comes from changes in cerebral hemodynamics, such as blood flow (CBF), blood volume (CBV), and blood oxygenation (CMRO2) that microscopically distorts the magnetic field. This introduces dephasing of the spatially local magnetization, causing temporally varying contrast changes in  $T_2^*$ -weighted magnitude images [1], [2]. While the hemodynamics are not a direct measure of neuronal activity, a strong relationship exists between the two [3]–[5].

Manuscript received September 21, 2007; revised December 17, 2007. First published February 2, 2008; current version published August 27, 2008. This work was supported by the National Institutes of Health under Grant EB02683 and Grant DA15410. Asterisk indicates corresponding author.

\*V. Olafsson is with the Department of Electrical Engineering and Computer Science, The University of Michigan, 2360 Bonisteel Blvd., Ann Arbor, MI 48109 USA (e-mail: volafss@umich.edu).

D. C. Noll is with the Biomedical Engineering Department, The University of Michigan, Ann Arbor, MI 48109 USA (e-mail: dnoll@umich.edu).

J. A. Fessler is with the Department of Electrical Engineering and Computer Science, The University of Michigan, Ann Arbor, MI 48109 USA (e-mail: fessler@umich.edu).

Color versions of one or more of the figures in this paper are available online at <http://ieeexplore.ieee.org>.

Digital Object Identifier 10.1109/TMI.2008.917247

Hence, brain function can be spatially mapped by acquiring multiple  $T_2^*$ -weighted time frames of a subjects brain, that has been instructed to perform some task, followed by statistical detection.

While  $T_2^*$ -weighted magnitude images give a qualitative measure of BOLD contrast, they are not quantitative in terms of the cerebral hemodynamics. However, the BOLD contrast can also be represented by the signal relaxation rate map  $R_2^* \triangleq 1/T_2^*$  [6], [7]. The  $R_2^*$  map expresses the signal relaxation that occurs during readout due to intravoxel dephasing of magnetization. It is quantifiable, i.e., has units of 1/s, and can be related to cerebral hemodynamics such as CBF, CBV, and CMRO2 [8]–[10]. This makes it an attractive method to map the observed BOLD contrast to the underlying mechanisms that drive it.

A complication of using  $R_2^*$  maps for fMRI is the nonlinear relationship it has to the acquired MR data. Models for  $R_2^*$  relaxation in the MR signal equation have included a bi-exponential relaxation model [11] and, in the presence of background gradients, a mono-exponential with a quadratic exponent [12] or a logspline density function [13]. However, in the absence of these gradients and for conventional resolutions and acquisition times used in current fMRI studies,  $R_2^*$  relaxation has been shown both in simulations [6] and *in vivo* experiments [7], [14]–[16] to approximate a mono-exponential behavior. Although this models the relaxation adequately, the relationship between  $R_2^*$  and acquired MR data is still nonlinear. This makes the problem of reconstructing  $R_2^*$  maps more difficult than if the relationship were linear, as is the case for  $T_2^*$ -weighted images.

To simplify  $R_2^*$  calculation, most studies that have used  $R_2^*$  maps for fMRI [7], [14], [17]–[20] have assumed models in which mono-exponential  $R_2^*$  relaxation occurs instantaneously at the echo time (TE), ignoring  $R_2^*$  relaxation during the MR signal readout. Hence, conventional  $R_2^*$  mapping involves multiple readouts with different echo times from which multiple  $T_2^*$ -weighted images are reconstructed followed by voxel-wise exponential decay fits. This process requires time consuming data collection and limits the spatial coverage and/or temporal resolution for  $R_2^*$  based fMRI. This can be improved by using partial parallel imaging such as SENSE [21] or GRAPPA [22] but with some loss of signal-to-noise ratio (SNR). In contrast, conventional  $T_2^*$ -weighted images require only a single readout which, along with the inability of conventional fMRI analysis tools to handle multiecho fMRI data, has made  $R_2^*$  estimates less popular than  $T_2^*$ -weighted images for fMRI.

Areas in the brain that have high susceptibility differences, such as air and tissue interfaces, are a source of off-resonance in fMRI imaging. This can lead to distortions in reconstructed  $T_2^*$ -weighted MR images. These degradations can be partially corrected using field map corrected reconstruction algorithms

[23]–[27]. Prior to employing these reconstructions the field map is conventionally estimated from additional data [28], [29], collected at the beginning of the fMRI study. This “static” field map is then used to reconstruct all the images collected during the study.

While acquiring fMRI data the magnetic field can drift and fluctuate causing temporal changes in the field map that are ignored in “static” field map corrected image reconstruction. Such temporal changes arise from heating in passive shim elements in the scanner bore, motion and physiological processes such as respiration [30], [31]. These temporal changes can be partially corrected in real time while collecting the MR data using navigators [32] or in the image reconstruction by updating the field map either before reconstructing each time frame or jointly [33]–[38]. However, the navigators correct only for spatially global off-resonance changes and even though updating the field map gives a voxel-based correction of the off-resonance, the image reconstruction methods are based on nonlinear iterative algorithms that can converge slowly.

Recently fast iterative field map corrected image reconstruction algorithms to solve linear problems have grown in popularity within the MRI community [26], [27]. These algorithms are versatile in dealing with non-Cartesian sampled MR data, with no need to estimate density compensation functions (DCF), and are easily extendable to correct for  $R_2^*$  relaxation and off-resonance. Also, iterative reconstruction algorithms can include regularization functions to control for bias and variance of the reconstructed images. Local point spread functions [39] have been used to investigate the local resolution properties of the reconstructed images. This information can be used to design regularizers for which the reconstructed images have a predetermined resolution that is spatially uniform [40]. The design must precede image reconstruction so it is desirable for it to be computationally efficient.

Here, we propose a method for fast joint reconstruction of  $R_2^*$  and field maps from MR data collected during an fMRI study. We use the mono-exponential relaxation model for  $R_2^*$  enabling us to combine  $R_2^*$  and field map into a single complex-valued map (Section II). We then linearize the MR signal equation relative to the temporal dynamics of this map and employ fast regularized iterative algorithms to reconstruct the complex-valued map (Section III). We also analyze the resolution properties of the reconstruction method and design a penalty to achieve approximately spatially uniform resolution for the reconstructed images (Section IV). We then simulate fMRI data for analysis and collect *in vivo* fMRI data for qualitative purposes (Sections VI and VII). For simplicity, motion is excluded from the reconstruction algorithm and the simulations.

## II. JOINT RECONSTRUCTION OF $R_2^*$ AND FIELD MAP

In fMRI the received complex-valued and discrete  $T_2^*$ -weighted MR data  $\mathbf{y} = [y_1, \dots, y_M]$ , including effects of mono-exponential relaxation and off-resonance, can be modeled as follows [6]:

$$y_m = s(t_m) + \epsilon_m, \quad m = 1, \dots, M \quad (1)$$

$$s(t) = \int f(\vec{r}) e^{-tz(\vec{r})} e^{-i2\pi(\vec{k}(t) \cdot \vec{r})} d\vec{r} \quad (2)$$

where  $\epsilon_m$  denotes complex-valued independent and identically distributed (i.i.d.) Gaussian noise [41] and  $s(t_m)$  is a sample of the MR signal equation defined in (2). In (2),  $\vec{r}$  is a 2-D or 3-D image space coordinate,  $f(\vec{r})$  is the magnetization of the object directly after excitation,  $\vec{k}(t)$  is the  $k$ -space trajectory used to acquire the MR data, and  $z(\vec{r})$  is a complex-valued spatial map

$$z(\vec{r}) = z_R(\vec{r}) + iz_I(\vec{r})$$

where the  $R_2^*$  map  $z_R(\vec{r})$  and the field map  $z_I(\vec{r})$  characterize the relaxation rate and off-resonance effects respectively for  $T_2^*$ -weighted images. Here, we would like to reconstruct  $z(\vec{r})$  from  $\mathbf{y}$ .

Reconstructing the continuous-space map  $z(\vec{r})$  from the discrete MR data  $\mathbf{y}$  using (2) is an ill-posed inverse problem. To simplify the problem, we parametrize  $f(\vec{r})$  and  $z(\vec{r})$  with the following approximations [26]:

$$\begin{aligned} z(\vec{r}) &\approx \sum_{n=1}^N z(\vec{r}_n) b(\vec{r} - \vec{r}_n) \\ f(\vec{r}) &\approx \sum_{n=1}^N f(\vec{r}_n) b(\vec{r} - \vec{r}_n) \end{aligned} \quad (3)$$

where  $b(\cdot)$  is the voxel basis function, chosen here as the 2-D or 3-D rect function. Using this in (2) gives

$$\begin{aligned} s(t; \mathbf{z}, \mathbf{f}) &\triangleq \Phi(\vec{k}(t)) \sum_{n=1}^N f(\vec{r}_n) e^{-tz(\vec{r}_n)} e^{-i2\pi(\vec{k}(t) \cdot \vec{r}_n)} \\ \mathbf{z} &\triangleq [z(\vec{r}_1), \dots, z(\vec{r}_N)] \\ \mathbf{f} &\triangleq [f(\vec{r}_1), \dots, f(\vec{r}_N)] \end{aligned} \quad (4)$$

where  $s(t; \mathbf{z}, \mathbf{f})$  is the discrete-space MR signal equation and  $\Phi(\vec{k}(t))$  is the Fourier transform of  $b(\cdot)$ . This form of the signal equation can now be used to reconstruct a discrete image  $\mathbf{z}$  from  $\mathbf{y}$ . Note that  $\mathbf{f}$  is generally not known and thus either needs to be determined before  $\mathbf{z}$  is reconstructed or jointly reconstructed with  $\mathbf{z}$  using (4).

In an fMRI study, a series of time frames are collected in an MRI scanner, where a frame can either be an image slice (2-D) or volume (3-D). Using (1) and (4), we model the received fMRI data for time frame  $j$  as follows:

$$\begin{aligned} \mathbf{y}_j &= \mathbf{s}(\mathbf{z}_j, \mathbf{f}) + \boldsymbol{\epsilon}_j, \quad j = 1, \dots, J \\ \mathbf{s}(\mathbf{z}_j, \mathbf{f}) &\triangleq [s(t_1; \mathbf{z}_j, \mathbf{f}), \dots, s(t_M; \mathbf{z}_j, \mathbf{f})] \end{aligned} \quad (5)$$

where  $\mathbf{y}_j$  is the received MR data,  $\mathbf{s}(\mathbf{z}_j, \mathbf{f})$  is the discrete MR signal from (4) and  $\boldsymbol{\epsilon}_j$  is i.i.d. Gaussian noise. An assumption in (5) is that  $\mathbf{f}$  is not time frame dependent, which in the absence of motion is reasonable for single shot MR data acquired using low-flip angles and/or long TRs to control for blood inflow enhancement [7]. Since  $\mathbf{f}$  is time frame independent, it can be reconstructed from specifically collected MR data  $\mathbf{y}_0$  prior to the fMRI acquisition. The reconstructed  $\mathbf{f}$  is denoted  $\hat{\mathbf{f}}$ .

Using  $\hat{\mathbf{f}}$  we can reconstruct  $\mathbf{z}_j$  from  $\mathbf{y}_j$  for  $j = 1, \dots, J$  by minimizing a penalized likelihood cost function as follows:

$$\begin{aligned} \Psi(\mathbf{z}_j) &= \frac{1}{2} \|\mathbf{y}_j - \mathbf{s}(\mathbf{z}_j)\|^2 + R(\mathbf{z}_j) \\ \hat{\mathbf{z}}_j &= \arg \min_{\mathbf{z}_j} \Psi(\mathbf{z}_j) \end{aligned} \quad (6)$$

where  $\mathbf{s}(z_j) \triangleq \mathbf{s}(z_j, \hat{\mathbf{f}})$ ,  $\hat{z}_j$  is the reconstructed  $z_j$  and  $R(z_j)$  is an appropriately chosen roughness penalty (see Section III-A) that controls the tradeoff between spatial resolution and noise in  $\hat{z}_j$ . The cost function  $\Psi(z_j)$  is nonconvex and would require a nonlinear iterative minimization algorithm, e.g., [35]–[38]. Any algorithm used to minimize it is likely to return a local minimum and thus needs to be carefully initialized.

We propose to solve (6) by converting it to a sequence of quadratic optimization problems so that fast iterative reconstruction algorithms can be used. The idea is to use a linear approximation to the dynamic temporal changes between  $z_j$  and a carefully chosen reference  $\check{z}$ . The advantage of using a sequence of quadratic approximations is that for each one, we can precompute temporal interpolators required for fast field-corrected image reconstruction [26], and then minimize that quadratic by nonuniform fast Fourier transform (NUFFT) or Toeplitz methods [27]. In contrast, if we apply gradient descent or conjugate gradient (CG) directly to (6), each gradient calculation would need new temporal interpolator coefficients, significantly increasing the computation time per iteration.

### III. DYNAMIC $z_j$ RECONSTRUCTION

This section describes an efficient algorithm for (6). Suppose a previously reconstructed reference map  $\check{z}$  is available (see discussion later in this section) in addition to  $\hat{\mathbf{f}}$ . Under this assumption, adding and subtracting  $\check{z}$  in the exponent containing  $z_j$  in (4) gives the following:

$$s(t; z_j) = \Phi(\vec{k}(t)) \sum_{n=1}^N \hat{f}(\vec{r}_n) e^{-t\check{z}(\vec{r}_n)} \times e^{-t(z_j(\vec{r}_n) - \check{z}(\vec{r}_n))} e^{-i2\pi(\vec{k}(t) \cdot \vec{r}_n)} \quad (7)$$

where the exponential has been split into two separate exponentials with one containing the difference of  $\check{z}$  and  $z_j$ . When this difference is small, that term can be approximated using a first-order Taylor expansion, as follows:

$$e^{-t(z_j(\vec{r}_n) - \check{z}(\vec{r}_n))} \approx 1 - t(z_j(\vec{r}_n) - \check{z}(\vec{r}_n)). \quad (8)$$

Substituting this in (7) yields

$$s(t; z_j) \approx s(t; \check{z}) + \Phi(\vec{k}(t)) \sum_{n=1}^N \hat{f}(\vec{r}_n) e^{-t\check{z}(\vec{r}_n)} \times (-t)(z_j(\vec{r}_n) - \check{z}(\vec{r}_n)) e^{-i2\pi(\vec{k}(t) \cdot \vec{r}_n)}. \quad (9)$$

Using the approximation in (8) the relationship of  $s(t; z_j)$  to  $z_j$  is now approximately linear (or more precisely affine) according to (9). This allows us to rewrite (9) in a matrix-vector form as follows:

$$\begin{aligned} \mathbf{s}(z_j) &\approx \mathbf{s}(z_j; \check{z}) \\ \mathbf{s}(z_j; \check{z}) &\triangleq \mathbf{s}(\check{z}) + \mathbf{A}(\check{z})(z_j - \check{z}) \end{aligned} \quad (10)$$

where  $\mathbf{A}(\cdot)$  is the *system matrix* of size  $M \times N$ , with elements written as follows:

$$a_{mn}(\check{z}) = \Phi(\vec{k}(t_m)) \hat{f}(\vec{r}_n) e^{-t_m \check{z}(\vec{r}_n)} (-t_m) e^{-i2\pi(\vec{k}(t_m) \cdot \vec{r}_n)}. \quad (11)$$

Using the approximation in (10), we can now approximate the difference of  $\mathbf{y}_j$  and  $\mathbf{s}(z_j)$ , as follows:

$$\begin{aligned} \mathbf{y}_j - \mathbf{s}(z_j) &\approx \mathbf{y}_j - \mathbf{s}(z_j; \check{z}) \\ &= \tilde{\mathbf{y}}_j(\check{z}) - \mathbf{A}(\check{z})z_j \end{aligned} \quad (12)$$

where

$$\tilde{\mathbf{y}}_j(\check{z}) \triangleq \mathbf{y}_j - \mathbf{s}(\check{z}) + \mathbf{A}(\check{z})\check{z}.$$

Using the approximation in (12) we can form a new cost function as follows:

$$\Psi(z_j; \check{z}) = \frac{1}{2} \|\tilde{\mathbf{y}}_j(\check{z}) - \mathbf{A}(\check{z})z_j\|^2 + R(z_j) \quad (13)$$

where  $\Psi(z_j; \check{z})$  is quadratic in terms of the objective  $z_j$ . By minimizing  $\Psi(z_j; \check{z})$  one can then reconstruct  $z_j$  using fast iterative reconstruction algorithms such as [26] and [27]. How well that matches to the result of (6) depends on the approximation made in (8), i.e., we must find a  $\check{z}$  that is close enough to the true  $z_j$  so that (8) does not introduce too much error in (12).

As previously discussed, the MR data  $\mathbf{y}_0$  is already needed to get  $\hat{\mathbf{f}}$ . This data could be acquired so that  $z_0$  and  $\mathbf{f}$  are jointly reconstructed from  $\mathbf{y}_0$  [35], [36]. Thus, one might choose  $\check{z}$  to be the reconstructed map  $\hat{z}_0$ . This reference map would approximate the *baseline* state of  $R_2^*$  and field map. However, in an fMRI study at 3 T the voxels showing activation have  $z_R$  and  $z_I$  showing maximum temporal changes of approximately  $-2s^{-1}$  [15] and 3 Hz [38], respectively, for a 3-min scan relative to baseline. By using  $z_0$  as the reference map and for a typical single shot acquisition with a TE = 30 ms the normalized root mean square (NRMS) error for the approximation in (8) would at worst be  $\sim 15\%$ , which would be undesirably large.

A more appropriate choice is to dynamically update  $\check{z}$  using a previous estimate of  $z_j$ , where the estimate then gets gradually *refined*. To differentiate between the refinements we denote them as  $\hat{z}_j^{(l)}$ , where  $l$  is the refinement index. Thus, we choose  $\check{z}$  as  $\hat{z}_j^{(l-1)}$  when reconstructing  $\hat{z}_j^{(l)}$ , and if the total number of refinements are  $L$  we set

$$\hat{z}_j^{(0)} = \hat{z}_{j-1} = \hat{z}_{j-1}^{(L)}.$$

With this choice of  $\check{z}$ , (8) should have a smaller approximation error as  $l$  increases, and thus the approximation in (12) should improve when used in (13).

Including the refinement concept into the reconstruction algorithm, we rewrite (12) as follows:

$$\mathbf{y}_j - \mathbf{s}(z_j) \approx \tilde{\mathbf{y}}_j(\hat{z}_j^{(l-1)}) - \mathbf{A}(\hat{z}_j^{(l-1)})z_j.$$

Using this we reconstruct  $\hat{z}_j$  for  $j = 1, \dots, J$  by minimizing  $L$  quadratic cost function as follows:

$$\hat{z}_j^{(l)} = \arg \min_{z_j} \Psi(z_j; \hat{z}_j^{(l-1)}), \quad l = 1, \dots, L \quad (14)$$

where  $\Psi(z_j; \cdot)$  was defined in (13) and  $\hat{z}_j = \hat{z}_j^{(L)}$ . This form of the reconstruction algorithm is very flexible and should approximate well the results of the original nonlinear reconstruction problem given in (6).

### A. Roughness Penalty $R(z_j)$ and Its Implications on $\hat{z}_j$

We must choose a roughness penalty  $R(z_j)$  in (14). The conventional choice is given as follows:

$$\frac{1}{2}\beta\|\mathbf{C}z_j\|^2$$

where  $\beta$  is the regularization parameter and  $\mathbf{C}$  is a real-valued first-order difference matrix that evaluates the differences of neighboring pixels within a user specified neighborhood. If  $R(z_j)$  were defined as this penalty the real and imaginary parts of  $z_j$  would be penalized equally. However, because the field map  $z_I$  is usually smoother than the  $R_2^*$  map  $z_R$ , we choose to regularize these maps separately, as follows:

$$R(z_j) = \frac{1}{2} \left( \beta_1 \|\mathbf{C}z_{R_j}\|^2 + \beta_2 \|\mathbf{C}z_{I_j}\|^2 \right) \quad (15)$$

where  $\mathbf{C}$  is the first-order difference matrix and  $z_{R_j}$  and  $z_{I_j}$  are, respectively, the real and imaginary parts of  $z_j$ . Note that  $\mathbf{C}$  can be defined separately for  $z_{R_j}$  and  $z_{I_j}$ . This can have some advantages, e.g., defining  $\mathbf{C}$  for  $z_{I_j}$  as a second-order difference matrix as suggested in [29] while  $\mathbf{C}$  for  $z_{R_j}$  is a first-order difference matrix. However, for simplicity we chose to use the same matrix for both parameters.

As evident from (11) the elements of  $\mathbf{A}(\hat{z}_j^{(l-1)})$  depend on  $\hat{\mathbf{f}}$ , which has values near 0 outside the object. This relationship has the following consequences:

$$\forall n \text{ s.t. } \hat{f}(\vec{r}_n) \approx 0 \Rightarrow \left[ \mathbf{A} \left( \hat{z}_j^{(l-1)} \right) z_j \right]_n \approx 0, \forall z_j \in \mathbb{C}^N.$$

This implies that the roughness penalty  $R(z_j)$  becomes the dominant factor in  $\Psi(z_j; \hat{z}_j^{(l-1)})$  for spatial positions outside the object.

### B. Implementation of the Fast Iterative Algorithm

For fast minimization of  $\Psi(z_j; \hat{z}_j^{(l-1)})$  in (14) we use the CG method [42]. To reduce memory we never explicitly form the large matrix  $\mathbf{A}(\cdot)$ , rather we use a software object to represent this matrix.<sup>1</sup> This software uses fast methods such as FFT (for Cartesian  $k$ -space trajectories) or NUFFT (for non-Cartesian  $k$ -space trajectories) [43] and temporal segmentation [26], [27] to greatly decrease computation time. The total compute time of the reconstruction algorithm is then roughly  $L$  times longer than previous fast iterative algorithms used to reconstruct  $T_2^*$ -weighted images [26], [27].

The convergence of CG depends on how it is initialized. A common CG initialization is to set all the elements of the initial solution to zero. This is a convenient initialization, but does not exploit any prior knowledge of the solution of (14). Another CG initialization would be to use the conjugate phase (CP) [24] reconstructed  $z_j$ . This initializer was shown to improve the convergence of CG, compared to initializing with all zeros, when used to iteratively reconstruct an off-resonance corrected  $T_2^*$ -weighted image [26]. However, since  $\mathbf{A}(\hat{z}_j^{(l-1)})$  also includes  $R_2^*$  relaxation, CP is ineffective here.

<sup>1</sup>Software available at <http://www.eecs.umich.edu/~fessler/>

As previously stated,  $z_j$  should change only slightly between neighboring time frames and across refinements. Thus, it is advantageous to exploit this relatively gradual temporal change to initialize the CG algorithm sensibly. Hence, when we reconstruct  $\hat{z}_j^{(l)}$  the previous refinement  $\hat{z}_j^{(l-1)}$  is used to initialize CG.

## IV. RESOLUTION PROPERTIES: REGULARIZATION DESIGN

The resolution properties of  $\hat{z}_j^{(l)}$  are important to further understand the relationship of the regularization function in (15) and the spatial smoothness of  $\hat{z}_j^{(l)}$ . Local point spread functions (LPSF) [39] have been previously used to analyze this relationship, using the approximate local resolution properties of regularized reconstruction algorithms with parametrized object models [40] as in (3). This analysis will be used first, to check if the penalized reconstruction in (14) has uniform spatial resolution and, if needed, design a penalty to achieve such uniformity. Then it will be used to set  $\beta$  values to achieve a predetermined resolution that is quantified using the full-width at half-maximum (FWHM) of the LPSF.

### A. Resolution Analysis

We estimate  $\hat{z}_j^{(l)}$  by minimizing  $\Psi(z_j; \hat{z}_j^{(l-1)})$  in (14) with separate regularization of the real and imaginary parts per (15). The Appendix derives the LPSF for such reconstruction problems. If the LPSF can be shown to be shift invariant then the spatial resolution of  $\hat{z}_j^{(l)}$  is uniform and the resolution properties of the algorithm can be quantified approximately by evaluating the LPSF in (26) at a single spatial location. If both  $\mathbf{A}'\mathbf{A}$  and  $\mathbf{C}'\mathbf{C}$  are Toeplitz, then using (26) one can show that the LPSF is approximately locally shift invariant.

For the reconstruction method used in this paper  $\mathbf{C}'\mathbf{C}$  is Toeplitz but  $\mathbf{A}'\mathbf{A}$  is not as seen from (11). Thus, the LPSF is shift variant, which makes the resolution nonuniform for the usual first-order difference matrix  $\mathbf{C}$  in (15). Next, we propose a spatially variant penalty design that leads to approximately uniform local spatial resolution.

### B. Spatially Variant Penalty Design

Although  $\mathbf{A}'\mathbf{A}$  is not Toeplitz, using methods similar to those proposed in [40] we can find an approximation of the form

$$\mathbf{A}'\mathbf{A} \approx \mathbf{D}'\mathbf{G}'\mathbf{G}\mathbf{D} \quad (16)$$

where  $\mathbf{G}'\mathbf{G}$  is Toeplitz and  $\mathbf{D}$  is a real-valued and invertible matrix. Having found such an approximation, we introduce a spatially variant differencing matrix  $\tilde{\mathbf{C}}$ , as follows:

$$\tilde{\mathbf{C}} = \mathbf{C}\mathbf{D}. \quad (17)$$

By replacing  $\mathbf{C}$  with  $\tilde{\mathbf{C}}$  in (15) the stacked LPSF in (26) becomes as follows:

$$l_{S_n} = (\mathbf{A}'_S \mathbf{A}_S + \tilde{\mathbf{C}}'_S \tilde{\mathbf{C}}_S)^{-1} \mathbf{A}'_S \mathbf{A}_S e_{S_n} \quad (18)$$

$$\begin{aligned} &\approx d_n \mathbf{D}_S^{-1} (\mathbf{G}'_S \mathbf{G}_S + \mathbf{C}'_S \mathbf{C}_S)^{-1} \mathbf{G}'_S \mathbf{G}_S e_{S_n} \\ &\approx (\mathbf{G}'_S \mathbf{G}_S + \mathbf{C}'_S \mathbf{C}_S)^{-1} \mathbf{G}'_S \mathbf{G}_S e_{S_n} \end{aligned} \quad (19)$$

where  $\mathbf{A}_S$  and  $\mathbf{e}_{S_n}$  are shown in (27),  $\tilde{\mathbf{C}}_S$  is a block diagonal matrix with  $\sqrt{\beta_1}\tilde{\mathbf{C}}$  and  $\sqrt{\beta_2}\tilde{\mathbf{C}}$  forming the diagonal blocks,  $d_n$  is the  $n$ th diagonal element of  $\mathbf{D}$  and

$$\mathbf{G}'_S \mathbf{G}_S = \begin{bmatrix} \Re(\mathbf{G}'\mathbf{G}) & -\Im(\mathbf{G}'\mathbf{G}) \\ \Im(\mathbf{G}'\mathbf{G}) & \Re(\mathbf{G}'\mathbf{G}) \end{bmatrix}$$

$$\mathbf{D}_S = \begin{bmatrix} \mathbf{D} & \mathbf{0} \\ \mathbf{0} & \mathbf{D} \end{bmatrix}.$$

Thus, even though  $\mathbf{A}'\mathbf{A}$  is not Toeplitz we can still make the LPSF to be approximately locally shift invariant by introducing a spatially variant penalty of the form (17) in the reconstruction.

We use a diagonal matrix  $\mathbf{D}$  such that the diagonal of  $\mathbf{A}'\mathbf{A}$  and  $\mathbf{D}'\mathbf{G}'\mathbf{G}\mathbf{D}$  are equal. This equality constraint when estimating  $\hat{\mathbf{z}}_j^{(l)}$  can be written as follows:

$$\sum_{m=1}^M \left| a_{mn} \left( \hat{\mathbf{z}}_j^{(l-1)} \right) \right|^2 = d_n \left( \hat{\mathbf{z}}_j^{(l-1)} \right)^2 \cdot \sum_{m=1}^M |g_{mn}|^2. \quad (20)$$

To find  $d_n$  we need to define  $g_{mn}$  such that  $\mathbf{G}'\mathbf{G}$  is Toeplitz and yet ensure (16) is a good approximation. The term in  $\mathbf{A}$  that makes  $\mathbf{A}'\mathbf{A}$  non-Toeplitz is  $\hat{f}(\vec{r}_n) e^{-t_m \hat{\mathbf{z}}_j^{(l-1)}(\vec{r}_n)}$ . Even though  $\hat{f}(\vec{r}_n)$  can be separated from  $\mathbf{A}'\mathbf{A}$  as proposed in (16) the same cannot be said for  $e^{-t_m \hat{\mathbf{z}}_j^{(l-1)}(\vec{r}_n)}$  because of its spatio-temporal structure. However, by approximating the elements of  $\hat{\mathbf{z}}_j^{(l-1)}$  with the median value of  $\hat{\mathbf{z}}_0$ , denoted  $\bar{z}$ , we define the elements of  $\mathbf{G}$  as follows:

$$g_{mn} \triangleq \Phi(\vec{k}(t_m)) e^{-t_m \bar{z}} (-t_m) e^{-i2\pi(\vec{k}(t_m) \cdot \vec{r}_n)}. \quad (21)$$

This definition of  $\mathbf{G}$  makes  $\mathbf{G}'\mathbf{G}$  Toeplitz and the diagonal elements of  $\mathbf{D}(\hat{\mathbf{z}}_j^{(l-1)}) = \mathbf{D}$  are then given as follows:

$$d_n(\hat{\mathbf{z}}_j^{(l-1)}) = |f(\vec{r}_n)| \sqrt{\frac{\sum_{m=1}^M c_m^2 e^{-2t_m \hat{\mathbf{z}}_j^{(l-1)}(\vec{r}_n)}}{\sum_{m=1}^M c_m^2 e^{-2t_m \bar{z}}}} \quad (22)$$

with  $c_m \triangleq \Phi(\vec{k}(t_m)) t_m$ . Note that this form of  $\mathbf{D}$  allows us to use (19) to find a single pair of regularization parameters to achieve a desired resolution that depends only on  $\hat{\mathbf{z}}_0$ .

### C. Spatially Variant Penalty Implementation

To implement the penalty designed in (22) there were some issues regarding computational speed and stability of the reconstruction that needed to be addressed.

- For stability, we find  $\mathbf{D}$  according to (22) at the beginning of the algorithm after estimating  $\hat{\mathbf{z}}_0$  and use that for subsequent  $j$  and  $l$ , i.e.,  $\mathbf{D}(\hat{\mathbf{z}}_j^{(l-1)}) \triangleq \mathbf{D}(\hat{\mathbf{z}}_0)$  for all  $(l, j)$ .
- Calculating (22) for all  $n$  is computationally expensive due to the spatio-temporal dependence of the numerator. However, since an  $R_2^*$  map generally has values within a fairly tight range we approximate the numerator by histogramming  $\hat{\mathbf{z}}_0$ .
- Our implementation of the penalty suggested in (17) uses the modification given in (35) in [40].
- Equation (19) is implemented efficiently using FFTs [44]. This allows us to evaluate it for multiple  $\beta$  values, calculate the FWHM of the resulting LPSFs and interpolate that to

the desired FWHMs and their associated  $\beta$  values in a fast manner.

## V. RECONSTRUCTION ALGORITHM—OVERVIEW

We can now summarize the proposed reconstruction algorithm as follows.

- Find  $\hat{\mathbf{f}}$  and  $\hat{\mathbf{z}}_0$  from multiecho MR data  $\mathbf{y}_0$  that is collected at the beginning of the fMRI study.
- Using (19), find  $\beta_1$  and  $\beta_2$  that yield the desired resolution for the real and imaginary parts of  $\hat{\mathbf{z}}_j$ .
- Generate  $\mathbf{D}$  for the regularizer using (22) with  $\hat{\mathbf{z}}_0$ .
- Reconstruct  $\hat{\mathbf{z}}_j$  for all  $j = 1, \dots, J$  as follows:
 

```

for  $j = 1, \dots, J$       [time]
  Set  $\hat{\mathbf{z}}_j^{(0)} = \hat{\mathbf{z}}_{j-1}$ .
  for  $l = 1, \dots, L$     [refinement]
    Form  $\mathbf{A}(\hat{\mathbf{z}}_j^{(l-1)})$  and generate  $\mathbf{s}(\hat{\mathbf{z}}_j^{(l-1)})$ .
    Solve  $\hat{\mathbf{z}}_j^{(l)} = \arg \min_{\mathbf{z}_j} \Psi(\mathbf{z}_j; \hat{\mathbf{z}}_j^{(l-1)})$  using CG.
  end
  Set  $\hat{\mathbf{z}}_j = \hat{\mathbf{z}}_j^{(L)}$ .
end

```

## VI. SIMULATIONS

We simulated  $k$ -space data using the exact form of the signal equation given in (4), with no temporal interpolation. We used a 4713 sample spiral-out  $k$ -space trajectory with a readout of 18.8 ms, FOV of 22 cm, and maximum gradient amplitude and slew rate of 22 mT/m and 180 mT/m/ms, respectively. The simulation maps were  $128 \times 128$  but reconstructed as  $64 \times 64$ , unless otherwise noted, with the baseline maps  $\mathbf{f}$  and  $\mathbf{z}_0$  shown in Fig. 1(a)–(c). For simulations corrupted by noise, we found the variance of the i.i.d. Gaussian noise to make the SNR 80, 55, or 30 for the baseline  $k$ -space data with TE = 30 ms, where:

$$\text{SNR} = \frac{\|\mathbf{s}(\mathbf{z}_0, \mathbf{f})\|}{\|\epsilon_0\|}.$$

This noise variance was then used to generate i.i.d. Gaussian noise for  $k$ -space data of other time frames and TEs.

For the iterative algorithm parameters we used nine segments for the temporal segmentation of  $e^{-tz(\vec{r}_n)}$ , which were interpolated using min-max interpolation coefficients [26]. When comparing the exact and interpolated complex exponential the maximum error and normalized RMS error (NRMSE) were on the order of  $10^{-7}$  and  $10^{-8}$  respectively for the simulation maps shown in Fig. 1(b)–(c). For the NUFFT parameters we used  $2 \times$  oversampling and a  $5 \times 5$  neighborhood [43]. We ran 20 iterations of CG for each  $(l, j)$  pair to get  $\hat{\mathbf{z}}_j^{(l)}$  and used a reconstruction mask to reduce the number of reconstructed voxels from 4096 to 2404. Fig. 1(a) shows the edge of the reconstruction mask. All reconstructions were run on a 2.13 GHz Intel Core 2 Duo with 2 GB of memory.

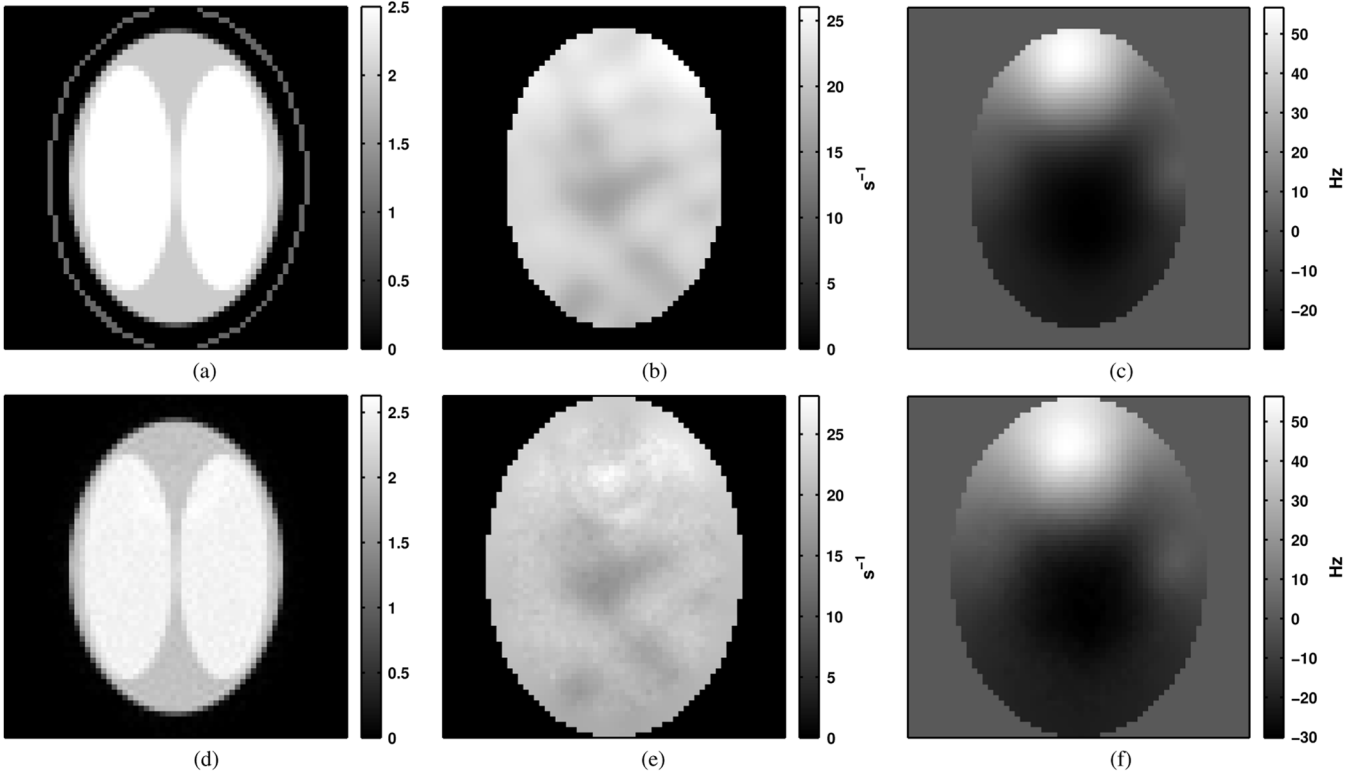


Fig. 1. True and reconstructed maps (SNR = 55) used in the simulations. (a)  $\mathbf{f}$  with the edge of the reconstruction mask for reference. (b)  $\mathbf{z}_{R_0}$ . (c)  $\mathbf{z}_{I_0}$ . (d)  $\hat{\mathbf{f}}$ . (e)  $\hat{\mathbf{z}}_{R_0}$ . (f)  $\hat{\mathbf{z}}_{I_0}$ . The reconstructed maps for simulated  $k$ -space data are only shown for voxels within the reconstruction mask and the (N)RMSE is the (normalized) rms error of the reconstructed map relative to the true map within the mask  $|\mathbf{f}| > 0$  for SNR = (80, 55, 30). (d) NRMSE = (3.9, 5.3, 8.8)%. (e) RMSE = (0.61, 0.66, 0.85) $s^{-1}$ . (f) RMSE = (0.30, 0.41, 0.70) Hz.

### A. Initialization: Estimating $\hat{\mathbf{f}}$ and $\hat{\mathbf{z}}_0$

The proposed reconstruction needs  $\hat{\mathbf{f}}$  and  $\hat{\mathbf{z}}_0$  for initialization. These spatial maps were reconstructed from multiple fully sampled readouts, i.e., *multiecho data*. Here, we simulated 5 echos with noise, where the readouts had TE = [6.5, 4.5, 24.3, 44.1, 63.8] ms. We reconstructed two  $T_2^*$ -weighted images from the 4.5 and 6.5 ms readouts using iterative reconstruction [26] and then estimated  $\hat{\mathbf{z}}_{I_0}$  from the phase difference of these two images [28], [29]. This was repeated two times, where after estimating  $\hat{\mathbf{z}}_{I_0}$  the first time it was used in the iterative reconstruction to correct for off-resonance during readout.

Using  $\hat{\mathbf{z}}_{I_0}$ , we reconstructed an off-resonance corrected  $T_2^*$ -weighted image for each echo of the multiecho data using the same iterative reconstruction. The reconstructed images have different  $T_2^*$ -weighting which is assumed to occur at TE. This allowed us to fit the decay of each voxel in the reconstructed images to a mono-exponential model [14], which gave  $\hat{\mathbf{z}}_{R_0}$ . Since this fit is highly sensitive to noise in voxels with low SNR, spatially weighted smoothing was performed that applied low smoothing to  $\hat{\mathbf{z}}_{R_0}$  in areas inside the object and higher smoothing where there are signal voids and outside the object, similar to [29]. We chose the weights as the magnitude image with TE = 4.5 ms. This was repeated three times, where after estimating  $\hat{\mathbf{z}}_{R_0}$  each time it was used in the iterative reconstruction to correct for  $R_2^*$  relaxation during readout.

From [14], we know that  $\hat{\mathbf{f}}$  could also be reconstructed using the mono-exponential fitting method. However, due to the poor

fitting performance in voxels with low SNR, we chose to reconstruct  $\hat{\mathbf{f}}$  iteratively using the signal model in (4) as follows:

$$\hat{\mathbf{f}} = \arg \min_{\mathbf{f}} \frac{1}{2} \|\mathbf{y}_0 - \mathbf{B}(\hat{\mathbf{z}}_0)\mathbf{f}\|^2 + \mathbf{R}(\mathbf{f})$$

where  $\mathbf{y}_0$  is the concatenated multiecho data,  $\mathbf{R}(\mathbf{f})$  is a roughness penalty and the elements of  $\mathbf{B}(\hat{\mathbf{z}}_0)$  are given as follows:

$$b_{mn}(\hat{\mathbf{z}}_0) = \Phi(\vec{k}(t_m))e^{-t_m \hat{\mathbf{z}}_0(\vec{r}_n)}e^{-i2\pi(\vec{k}(t_m) \cdot \vec{r}_n)}$$

where  $t_m$  are the concatenated time vector samples of the simulated readouts and  $\hat{\mathbf{z}}_0$  is formed using  $\hat{\mathbf{z}}_{R_0}$  and  $\hat{\mathbf{z}}_{I_0}$ . We chose the spatial regularization for  $\hat{\mathbf{f}}$  so that the LPSF of the center voxel had a FWHM of approximately 1.25 voxels.

The results for simulated  $k$ -space data with SNR = 55 are shown in Fig. 1(d)–(f) and the (N)RMSE shown below the images is the (normalized) RMS error of the reconstructed map relative to the true map within the mask  $|\mathbf{f}| > 0$  for all SNRs.

### B. Resolution: Properties and Nonuniformity Correction

Here, we analyze the performance of the proposed spatially variant penalty. All the analysis is based on the true simulation maps in Fig. 1(a)–(c). We started by finding  $\beta_1$  and  $\beta_2$  to achieve a desired resolution. We chose the desired resolution such that the LPSF for the center voxel gave a FWHM of 1.35 and 1.5 voxels for the real and imaginary parts of  $\hat{\mathbf{z}}_j^{(l)}$  respectively. This was done by evaluating the LPSF in (19) for 100 pairs of  $\beta_1$  and  $\beta_2$ , where  $\bar{\mathbf{z}}$  was the median of the true  $\mathbf{z}_0$  in Fig. 1(b)–(c). Using FFTs [44] it took 19.2 s to evaluate the LPSFs for all 100 pairs.

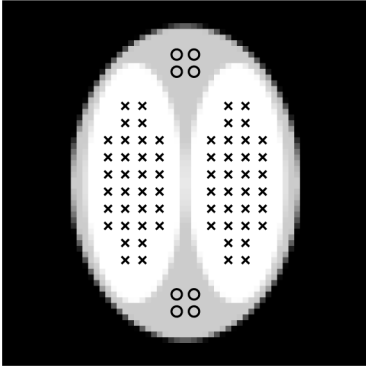


Fig. 2. Voxel positions where the LPSFs in (18) were evaluated. The positions are split into two groups, indicated by the x's and o's, where each group are at locations where the value of  $\mathbf{f}$  is the same.

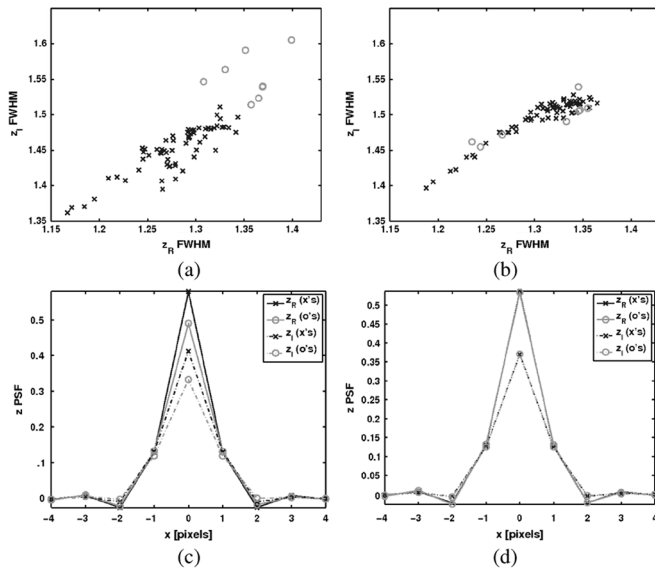


Fig. 3. FWHM scatter plots and average profile of the LPSF for the two groups of voxel positions in Fig. 2. Results are shown for the real and imaginary parts of  $\hat{z}_1$  when using the spatially variant and nonvariant penalty. (a) Scatter plot for spatially nonvariant penalty. (b) Scatter plot for spatially variant penalty. (c) Average profile for spatially nonvariant penalty. (d) Average profile for spatially variant penalty.

The FWHMs of those LPSFs were then used to interpolate the desired FWHM to their associated  $\beta$  values.

Using those  $\beta$  values, we calculated the exact LPSF using (18) at the voxel positions shown in Fig. 2. We investigated the resolution properties by evaluating (18) for  $\hat{z}_1$ , with  $\mathbf{A}_s$  formed by stacking  $\mathbf{A}(z_0)$  and using the true  $\mathbf{f}$  in place of  $\hat{\mathbf{f}}$ . The spatially variant penalty was formed in 4.7 s using (22), where the true simulation maps were again used and the numerator was calculated by histogramming  $z_{R_0}$  with 100 bins. For comparison, we also designed a spatially nonvariant penalty by making a diagonal matrix using the mean of  $d_n(z_0)$  in (22) across all voxels where  $|\mathbf{f}| > 0$ . This made the nonvariant penalty approximately have the desired FWHM using the previously calculated  $\beta$  values.

Fig. 3 shows both FWHM scatter plots and the average profile of the LPSF for the voxel positions in Fig. 2 of the real and

imaginary parts of  $\hat{z}_1$  for both penalties. The calculated FWHM values are more concentrated around the desired FWHM values when using the spatially variant penalty compared to the nonvariant one. This is further confirmed in the profile plots of the LPSFs averaged over each group for both the real and imaginary parts of  $\hat{z}_1$ . This indicates the importance of compensating for spatial resolution nonuniformity in the reconstruction algorithm.

Table I shows the mean and the standard deviation of the FWHM for both the real and imaginary parts of  $\hat{z}_1$ . It shows further evidence of the effect of  $\mathbf{f}$  in causing resolution nonuniformity in the reconstructed  $z_j$ . The mean FWHM of the two groups from Fig. 2 deviate more when using a spatially nonvariant penalty compared to the proposed penalty. Repeating these measurements for  $\mathbf{A}(\hat{z}_j)$  for a time frame  $j$  during activation the numbers did not change significantly while still using  $d_n(z_0)$  to form  $\mathbf{D}$ . This indicates that it is sufficient to find  $\mathbf{D}$  based on  $\hat{\mathbf{f}}$  and  $\hat{z}_0$  and use that for all time frames.

### C. Simulated fMRI Data

To analyze the proposed reconstruction in (14) for fMRI time series we compared its activation detection and  $R_2^*$  estimation performance to an iterative  $T_2^*$ -weighted reconstruction [26] and a multi-echo  $R_2^*$  reconstruction [14]. We simulated a 70 time frame four-echo fMRI data with  $\text{TE} = [10.2, 30, 49.8, 69.6]$  ms. The  $\text{TE} = 30$  ms readouts were used for the proposed and the  $T_2^*$ -weighted reconstructions. For the multiecho  $R_2^*$  reconstruction we iteratively reconstructed four  $T_2^*$ -weighted images [26], one for each readout, and estimated both  $R_2^*$  and  $\mathbf{f}$  by fitting a mono-exponential decay to each voxel of the  $T_2^*$ -weighted magnitude images.

Fig. 4 shows the simulated fMRI spatial activation map and the temporal changes. Fig. 4(a) shows the spatial weights for four enumerated activation clusters, along with the edges of  $\mathbf{f}$  in Fig. 1(a) shown for reference. Fig. 4(b) shows the task related temporal changes in  $z_R$  that were simulated in all the clusters. Additionally, in clusters 2 and 3 we added task correlated changes in  $\mathbf{f}$  and  $z_I$  respectively (maximum change of 1% and 0.15 rad/s). Cluster 1 was placed where the in-plane field map gradient of  $z_{I_0}$  was large, while cluster 4 was placed along the edge of  $\mathbf{f}$ . Fig. 4(c) shows the spatially global drift in  $z_I$  that simulates the effects of magnetic field drift and respiration. The  $k$ -space time series was generated by adding these spatio-temporal changes to  $z_0$  and  $\mathbf{f}$  in Fig. 1, using the exact MR signal (4) and noise.

To choose  $L$  for the proposed reconstruction, we generated noiseless  $k$ -space data from  $64 \times 64$  images to reconstruct  $\hat{z}_j$  with  $L = 1, \dots, 5$  by solving (14). The desired resolution was set as described in the first paragraph in Section VI-B and we used the true  $\mathbf{f}$  and  $z_0$  to exclude any effect from the initialization of the reconstruction. With the exception of the first time frame the algorithm had similar temporal RMSE for  $L \geq 2$  (average temporal RMSE was 0.197). Hence, we chose to use  $L = 5$  for the first time frame and  $L = 2$  for subsequent time frames when reconstructing the  $k$ -space data from  $128 \times 128$  images. We also initialized the reconstruction using  $\hat{\mathbf{f}}$  and  $\hat{z}_0$  from Section VI-A.

TABLE I  
AVERAGE FWHM FOR BOTH  $\hat{z}_{R_1}$  AND  $\hat{z}_{I_1}$  WITH ITS STANDARD DEVIATION FOR BOTH THE SPATIALLY NONVARIANT AND PROPOSED PENALTIES

	Spatially Nonvariant Penalty		Spatially Variant Penalty		Desired
	x's	o's	x's	o's	
$\hat{z}_{R_1}$ FWHM	$1.28 \pm 0.04$	$1.36 \pm 0.03$	$1.31 \pm 0.04$	$1.31 \pm 0.05$	1.35
$\hat{z}_{I_1}$ FWHM	$1.45 \pm 0.04$	$1.55 \pm 0.03$	$1.50 \pm 0.03$	$1.50 \pm 0.03$	1.50

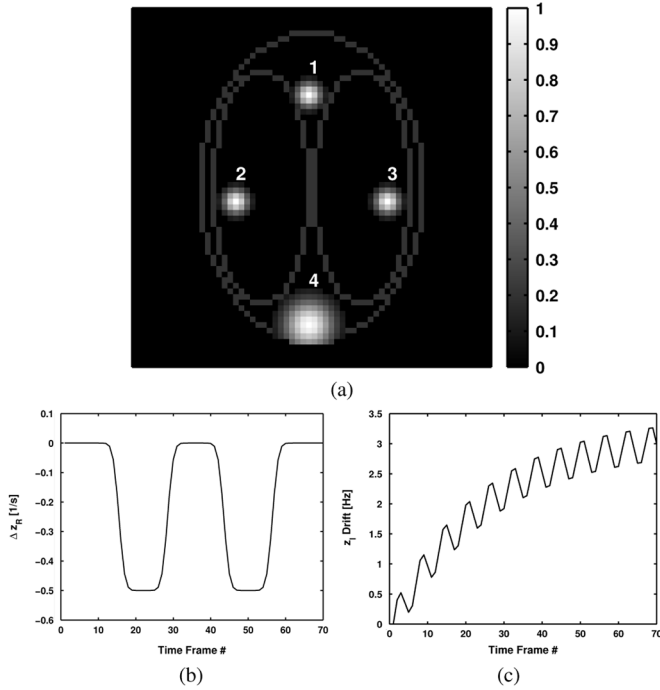


Fig. 4. Simulated spatial and temporal activations. (a) Map of the spatial weights for four enumerated activation clusters, along with the edges of  $\mathbf{f}$  in Fig. 1(a) shown for reference. (b) Additive task waveform for  $R_2^*$  for all clusters. Additionally, in clusters 2 and 3 we added task related changes in  $\mathbf{f}$  and  $z_1$  respectively (maximum change of 1% and 0.15 rad/s). (c) Additive spatially global drift in the field map to simulate the effects of magnetic field drift and respiration.

All the  $T_2^*$ -weighted reconstructed readouts used 20 CG iterations, with CG initialized using the conjugate phase reconstruction [24], and corrected for off-resonance in all time frames using  $\hat{z}_{I_0}$ . The regularization parameter was chosen to have a LPSF with FWHM of 1.35 so that the resolution was comparable to  $\hat{z}_{R_j}$  from the proposed reconstruction.

We reconstructed all the time frames for all SNRs. We did the time series analysis using a GLM model with the task waveform as a regressor and generated  $z$ -score maps that were thresholded with a Bonferroni corrected  $P$ -value of 0.01. Fig. 5 shows the overlaid  $z$ -score of the voxels inside  $\mathbf{f}$  that were above the threshold for SNR = 80 (left) and SNR = 30 (right). Voxels with true positives are shown with a color coded  $z$ -score and false negatives with an empty square. Fig. 5(a)–(b) shows the results from the dynamically reconstructed  $\hat{z}_j$ , Fig. 5(c)–(d) from the  $T_2^*$ -weighted reconstruction, and Fig. 5(e)–(f) from the multi-echo  $R_2^*$  reconstruction.

Fig. 5 shows that in terms of total number of true positives the four-echo  $R_2^*$  reconstruction performs the worst. This is especially apparent in cluster 1 due to the high in-plane field map gradient. Compared to the  $T_2^*$ -weighted reconstruction, the pro-

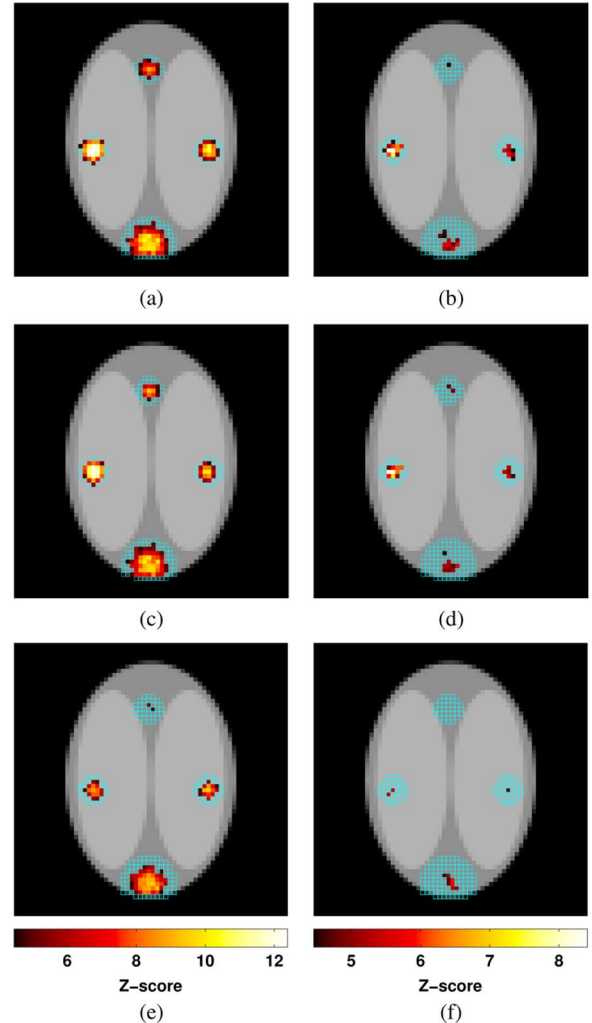


Fig. 5. Overlaid  $z$ -score of the voxels inside  $\mathbf{f}$  that were above the threshold (Bonferroni corrected  $P$ -value of 0.01) for SNR = 80 (left) and SNR = 30 (right). (a) and (b): Dynamic  $\hat{z}_{R_j}$  reconstruction. (c) and (d):  $T_2^*$ -weighted reconstruction. (e) and (f): Multiecho  $R_2^*$  reconstruction.

posed reconstruction performs slightly better for both SNRs, especially for voxels that have low functional CNR. This is particularly evident in cluster 3, that has the task correlated changes in the field map, and cluster 4. However, both these reconstructions are sensitive to the task correlated changes in  $\mathbf{f}$  for cluster 2. The multiecho  $R_2^*$  reconstruction is more robust to this effect. Similar trends are seen for SNR = 55 as for the other SNRs.

Fig. 6 shows  $R_2^*$  time series from the three reconstructions, spatially averaged over cluster 1-3, as shown in Fig. 6(a)–(c), respectively. For reference, the plots show the true spatially averaged  $z_{R_j}$  time series. To convert the  $T_2^*$ -weighted time series to  $R_2^*$  we calculated its  $\Delta R_2^*$  time series using  $\Delta R_2^* \approx$

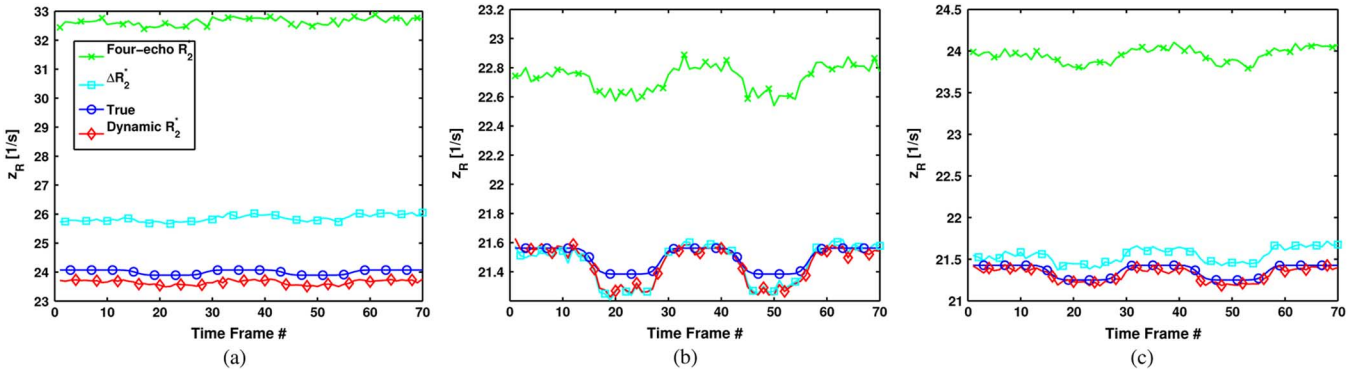


Fig. 6. Estimated  $R_2^*$  time series (SNR = 55) for all the reconstructions, which was spatially averaged over each cluster, along with the true  $z_{R,j}$ . (a) Results from cluster 1. (b) Results from cluster 2. (c) Results from cluster 3.

$-(S_j - S_1)/S_1/TE$ , where  $S_j$  is the  $T_2^*$ -weighted magnitude image of time frame  $j$ . This time series was then shifted by  $\hat{z}_{R_0}$ . The plots show that the multiecho  $R_2^*$  reconstruction performs the worst and the proposed reconstruction the best in estimating the  $R_2^*$  time series. This is obvious in Fig. 6(a) due to the high in-plane field map gradient of cluster 1. Fig. 6(b) shows how the simulated inflow changes in cluster 2 affect the  $R_2^*$  estimates during activation for both the proposed and  $T_2^*$ -weighted reconstructions. Additionally, all plots indicate a slight linear drift in the  $\Delta R_2^*$  time series, as clearly seen in Fig. 6(c). All the clusters have  $<2\%$  error in estimating  $R_2^*$  time series for the proposed reconstruction.

## VII. EXPERIMENTAL DATA

We scanned a single subject in an fMRI experiment to demonstrate the proposed reconstruction for *in vivo* data and compared with  $T_2^*$ -weighted and multiecho  $R_2^*$  reconstructions. The data had 102 time frames, four-echo spiral-out readouts, FOV = 24 cm, TR = 3.2 s, and FA = 90°. The first time frame had TE = [4.6, 23.2, 41.8, 60.4] ms, the second time frame the same TEs shifted by 2 ms, and subsequent time frames had TE = [11.4, 30, 48.6, 67.2] ms. The subject was instructed to repeat 5 times 32 s of rest followed by 32 s of bilateral finger tapping prompted by a flickering checkerboard. We collected 26 axial slices that covered the visual and motor cortices.

The four readouts from the first time frame and the first readout of the second time frame were used to form a five-echo  $k$ -space data with TE = [4.6, 6.6, 23.2, 41.8, 60.4] ms. This five-echo data was used to estimate  $\hat{f}$  and  $\hat{z}_0$  identically to the procedure described in Section VI-A. For the proposed and  $T_2^*$ -weighted reconstructions we used only the TE = 30 ms readout while the multiecho  $R_2^*$  reconstruction used all the readouts. All the reconstructions were set up identically to what was described in Section VI.

The fMRI analysis was applied to all the reconstructions, using a GLM model with a gamma-variate regressor [45] for the task and a linear regressor for the linear drift. We generated  $z$ -score maps that were thresholded using a Bonferroni corrected  $P$ -value of 0.01 followed by a clustering constraint [46] of at least one neighboring voxel above the threshold. Fig. 7 shows two slices with overlaid  $z$ -scores of voxels above the threshold for all the reconstructions. The left column of Fig. 7 shows a superior slice with motor activation and the right column shows an

inferior slice with visual activation. Fig. 7(a)–(b) shows the results from the proposed reconstruction, Fig. 7(c)–(d) from the  $T_2^*$ -weighted reconstruction, and Fig. 7(e)–(f) from the four-echo  $R_2^*$  reconstruction.

Fig. 7 shows clear activations in the motor cortex, supplementary motor area, and the visual cortex for all the reconstructions. Also,  $f$  estimates from the four-echo  $R_2^*$  reconstruction showed only three voxels in the visual cortex having minor task correlated inflow and none in the motor cortex. The results from the superior slice follows the trend shown in the simulations, where the proposed reconstruction has the most number of voxels classified as active and the four-echo  $R_2^*$  reconstruction the fewest. However, this is not the case for the inferior slice, where the  $T_2^*$ -weighted reconstruction has the most active voxels. This difference may be due to the stronger field gradients in the inferior slice that currently are not included in the signal model in (4).

## VIII. CONCLUSION AND DISCUSSION

We have proposed a method for reconstructing dynamic  $R_2^*$  and field maps for fMRI data with the same temporal resolution as  $T_2^*$ -weighted imaging. This was done using a linear approximation to the temporal changes in  $R_2^*$  and field maps relative to a previously determined reference map. Simulations showed the reconstruction outperformed both  $T_2^*$ -weighted and four-echo  $R_2^*$  reconstructions in detecting active voxels. For the quantitative  $R_2^*$  estimation the proposed reconstruction did considerably better than the four-echo  $R_2^*$  reconstruction but about the same as the  $T_2^*$ -weighted reconstruction after converting it to  $\Delta R_2^*$  and excluding the  $\hat{z}_{R_0}$  shift. However, there was a slight drift present in the  $\Delta R_2^*$  time series, which may explain the lower detection performance of the  $T_2^*$ -weighted reconstruction compared to the proposed reconstruction. Adding a linear drift regressor into the GLM model did improve the performance of the  $T_2^*$ -weighted reconstruction, but still not to the level of the proposed reconstruction.

For the *in vivo* data all the reconstructions showed a similar trend to the simulation results for the superior slice, less so for the inferior slice. Since the inferior slice is closer to the sinuses it is more affected by field gradients than the superior slice. The effects of the gradients are not in the signal equation for any of the reconstructions used here. However, when compared to  $T_2^*$ -weighted reconstruction, the proposed reconstruction does rely on a mono-exponential relaxation model which can introduce model bias in areas with high gradients [12], [13]. Adding

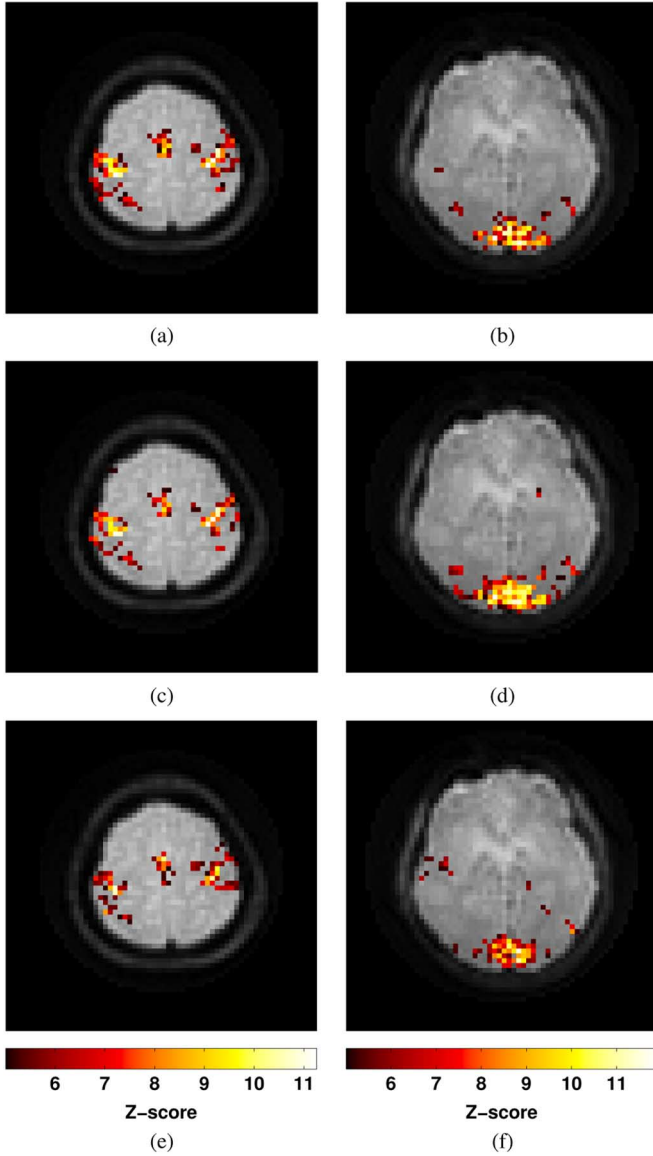


Fig. 7. Z-scores of voxels above the threshold for two slices overlaid on anatomical images for all the reconstructions. Left column shows the results of a superior slice with motor activation and right column shows the results of an inferior slice with visual activation. (a) and (b): Dynamic  $\hat{z}_j$  reconstruction. (c) and (d):  $T_2^*$ -weighted reconstruction. (e) and (f): Four-echo  $R_2^*$  reconstruction.

gradients in the signal equation in (4), [47] may also alleviate this model mismatch for the proposed reconstruction. This is something that needs further investigation. Any further comparisons in terms of detection performance for the *in vivo* data would need more acquisitions and estimation of test–retest reliability [48].

The compute time and the performance of the algorithm depends mainly on the number of refinements used to find  $\hat{z}_j$ . It was shown in the simulations that  $L = 5$  for the first time frame and  $L = 2$  for other time frames was adequate. The compute time for the first time frame was 60.3 s, which includes forming  $\mathbf{D}$  (4.7 s) and finding the  $\beta$  values to satisfy our desired resolution (19.2 s), and subsequent time frames took 17.7 s. This time could be reduced by reusing common parts of  $\mathbf{A}$  for all time frames. The reconstruction is then two times longer than  $T_2^*$ -weighted reconstruction since  $L = 2$ , but with the added benefit of correcting for field drift and getting  $R_2^*$  estimates.

Currently, the algorithm does not include any motion correction. Since all the simulations were done without motion the performance of the algorithm with motion has not been assessed. However, since it relies on the reconstructed map  $\hat{\mathbf{f}}$ , one would assume that any motion in the data is going to translate into changes in  $\hat{\mathbf{f}}$ . This may make the algorithm more sensitive to motion induced errors than  $T_2^*$ -weighted image reconstruction, where all the frames can be reconstructed independent of past or future time frames.

One simple method for motion correction would be to estimate rigid body motion parameters from  $T_2^*$ -weighted images, using the first time frame as the reference frame. We would then use those motion parameters when reconstructing  $\hat{z}_j$  for the same data to correct  $\hat{\mathbf{f}}$  in the system matrix for any motion. This method and others need to be investigated further but ultimately motion correction must be included in the algorithm for it to be robust.

In addition to excluding motion there is also an assumption of blood inflow being limited. Under this assumption  $\hat{\mathbf{f}}$  should be time frame invariant when reconstructing  $\hat{z}_j$  for all  $j$ . One way to limit the effects of inflow enhancement is to acquire the data by either increasing TR or decreasing the flip angle [7], which, respectively, puts limitations on the data acquisition and lowers SNR. This effect could also be decreased by jointly reconstructing  $\hat{\mathbf{f}}$  and  $\hat{z}_j$ . However, due to the higher dimensionality of this ill-conditioned reconstruction of both spatial maps, longer readouts and further regularization of  $\hat{\mathbf{f}}$  would be needed. This would potentially be at a cost of higher compute times due to the increased complexity.

In our nonuniform regularization design, there are mainly three limitations. First, we form the spatially nonuniform penalty once and then only based on  $\hat{z}_{R_0}$ . This can result in time frame varying resolution for voxels with significant temporal changes in  $z_j$ . Additionally, any spatial resolution variations due to  $\hat{z}_{I_j}$  are not compensated since we only account for spatial variations in  $R_2^*$ . Second, we chose the regularization parameter arbitrarily to satisfy a desired FWHM. There are alternative methods available to choose this parameter [49], such as cross validation. Third, since  $|\hat{\mathbf{f}}|$  is multiplicative in  $\mathbf{D}$ , voxels with low  $|\hat{\mathbf{f}}(\vec{r}_n)|$  will have very little regularization. This could be alleviated by smoothly extending high  $|\hat{\mathbf{f}}(\vec{r}_n)|$  voxels over the low valued voxels to decrease the variance of the estimates. These design limitations need further investigation, especially with respect to resolution uniformity, reconstruction compute time and bias/variance trade-off.

The simulated and *in vivo*  $k$ -space data was acquired using a single shot spiral-out trajectory. The accuracy of the algorithm does depend on the readout length of the trajectory that is used to acquire the data. For instance, a fully sampled single shot spiral-in followed by an undersampled spiral-out was shown to have higher correlation values than using only spiral-in data [50]. Further investigation of the behavior of the algorithm for various trajectories and readout lengths is needed.

To initialize the algorithm, we used data collected at the start of the fMRI study to reconstruct  $z_{I_0}$ , then  $z_{R_0}$ , and finally  $\mathbf{f}$ . The reconstruction of  $\hat{\mathbf{f}}$  may be sensitive to errors in  $\hat{z}_0$ , which may especially come from  $\hat{z}_{R_0}$  since log fitting is very sensitive to noise. An alternative solution would be to use a joint reconstruction algorithm [35], [36], where  $\hat{z}_0$  and  $\hat{\mathbf{f}}$  are simultaneously re-

constructed by minimizing one regularized cost function instead of minimizing separate cost functions for each spatial map.

#### APPENDIX A STACKED LPSF

It has been previously shown [40] that for a quadratic penalized likelihood (QPL) reconstruction using a roughness penalty that penalizes the real and imaginary parts equally

$$\hat{z} = \arg \min_z \frac{1}{2} \|\mathbf{y} - \mathbf{A}z\|^2 + \frac{1}{2} \beta \|\mathbf{C}z\|^2$$

the LPSF at spatial position  $n$  is given by

$$\mathbf{l}_n = (\mathbf{A}'\mathbf{A} + \beta\mathbf{C}'\mathbf{C})^{-1} \mathbf{A}'\mathbf{A}\mathbf{e}_n, n = 1, \dots, N \quad (23)$$

where  $\mathbf{l}_n$  is the LPSF and  $\mathbf{e}_n$  is a vector with 1 at vector element position  $n$  and zeros elsewhere (Kronecker impulse). However, for a QPL reconstruction using our preferred roughness penalty given in (15), where the real and imaginary parts are penalized separately

$$\hat{z} = \arg \min_z \frac{1}{2} \|\mathbf{y} - \mathbf{A}z\|^2 + \frac{1}{2} (\beta_1 \|\mathbf{C}z_R\|^2 + \beta_2 \|\mathbf{C}z_I\|^2) \quad (24)$$

the same analysis used in [40] to derive the LPSF does not apply. To analyze this situation, we introduce a “stacked” formulation in which the matrices and vectors are rewritten as follows:

$$\mathbf{y}_S = \begin{bmatrix} \mathbf{y}_R \\ \mathbf{y}_I \end{bmatrix}, \mathbf{A}_S = \begin{bmatrix} \mathbf{A}_R & -\mathbf{A}_I \\ \mathbf{A}_I & \mathbf{A}_R \end{bmatrix}$$

$$\mathbf{z}_S = \begin{bmatrix} \mathbf{z}_R \\ \mathbf{z}_I \end{bmatrix}, \mathbf{C}_S = \begin{bmatrix} \mathbf{C}_1 & 0 \\ 0 & \mathbf{C}_2 \end{bmatrix}$$

where the subscripts R and I refer to the real and imaginary part of the variable respectively and  $\mathbf{C}_1 = \sqrt{\beta_1}\mathbf{C}$  and  $\mathbf{C}_2 = \sqrt{\beta_2}\mathbf{C}$ , where  $\beta_1$  and  $\beta_2$  can be chosen independently. Using these definitions for the stacked matrices and vectors we can write the stacked QPL reconstruction in (24) as follows:

$$\hat{z}_S = \arg \min_{z_S} \frac{1}{2} \|\mathbf{y}_S - \mathbf{A}_S z_S\|^2 + \frac{1}{2} \|\mathbf{C}_S z_S\|^2. \quad (25)$$

Using the analysis that led to (23), the stacked LPSF  $\mathbf{l}_{S_n}$  for  $\hat{z}_S$  at spatial position  $n$  can be written as follows:

$$\mathbf{l}_{S_n} = (\mathbf{A}'_S \mathbf{A}_S + \mathbf{C}'_S \mathbf{C}_S)^{-1} \mathbf{A}'_S \mathbf{A}_S \mathbf{e}_{S_n}$$

$$n = 1, \dots, N \quad (26)$$

with

$$\mathbf{l}_{S_n} = \begin{bmatrix} \mathbf{l}_{R_n} \\ \mathbf{l}_{I_n} \end{bmatrix}$$

$$\mathbf{A}'_S \mathbf{A}_S = \begin{bmatrix} \Re(\mathbf{A}'\mathbf{A}) & -\Im(\mathbf{A}'\mathbf{A}) \\ \Im(\mathbf{A}'\mathbf{A}) & \Re(\mathbf{A}'\mathbf{A}) \end{bmatrix}$$

$$\mathbf{C}'_S \mathbf{C}_S = \begin{bmatrix} \mathbf{C}'_1 \mathbf{C}_1 & 0 \\ 0 & \mathbf{C}'_2 \mathbf{C}_2 \end{bmatrix}$$

$$\mathbf{e}_{S_n} = \begin{bmatrix} (1 - \alpha)\mathbf{e}_n \\ \alpha\mathbf{e}_n \end{bmatrix} \quad (27)$$

where  $\Re(\mathbf{A}'\mathbf{A})$  and  $\Im(\mathbf{A}'\mathbf{A})$  are the real and imaginary parts of  $\mathbf{A}'\mathbf{A}$ , respectively, and  $\alpha \in \{0, 1\}$  is used to select the stacked LPSF of the real or imaginary parts of  $z$ .

#### REFERENCES

- [1] S. Ogawa, T. Lee, A. Nayak, and P. Glynn, “Oxygenation-sensitive contrast in magnetic resonance image of rodent brain of high magnetic fields,” *Magn. Reson. Med.*, vol. 14, pp. 68–78, 1990.
- [2] S. Ogawa, T.-M. Lee, A. R. Kay, and D. W. Tank, “Brain magnetic resonance imaging with contrast dependent blood oxygenation,” in *Proc. Nat. Acad. Sci.*, Dec. 1990, vol. 87, no. 24, pp. 9868–9872.
- [3] K. K. Kwong, J. W. Belliveau, D. A. Chesler, I. E. Goldberg, R. M. Weisskoff, B. P. Poncelet, D. N. Kennedy, B. E. Hoppel, M. S. Cohen, R. Turner, H.-M. Cheng, T. J. Brady, and B. R. Rosen, “Dynamic magnetic resonance imaging of human brain activity during primary sensory stimulation,” in *Proc. Nat. Acad. Sci. USA*, Jun. 1992, vol. 89, no. 12, pp. 5675–5679.
- [4] S. Ogawa, D. W. Tank, R. Menon, J. M. Ellermann, S. Kim, H. Merkle, and K. Ugurbil, “Intrinsic signal changes accompanying stimulation: Functional brain mapping with magnetic resonance imaging,” in *Proc. Natl. Acad. Sci.*, Jul. 1992, vol. 89, no. 13, pp. 5951–5955.
- [5] P. A. Bandettini, E. C. Wong, R. S. Hinks, R. S. Tikofsky, and J. S. Hyde, “Time course EPI of human brain function during task activation,” *Magn. Reson. Med.*, vol. 25, pp. 390–397, 1992.
- [6] S. Ogawa, R. S. Menon, D. W. Tank, S. G. Kim, H. Merkle, J. M. Ellermann, and K. Ugurbil, “Functional brain mapping by blood oxygenation level-dependent contrast magnetic resonance imaging. A comparison of signal characteristics with a biophysical model,” *Biophys. J.*, vol. 64, no. 3, pp. 803–812, Mar. 1993.
- [7] J. S. Gati, R. S. Menon, K. Ugurbil, and B. K. Rutt, “Experimental determination of the BOLD field strength dependence in vessels and tissue,” *Mag. Res. Med.*, vol. 38, no. 2, pp. 296–302, Aug. 1997.
- [8] R. D. Hoge, J. Atkinson, B. Gill, G. R. Crelier, S. Marrett, and G. B. Pike, “Investigation of BOLD signal dependence on cerebral blood flow and oxygen consumption: The deoxyhemoglobin dilution model,” *Magn. Reson. Med.*, vol. 42, pp. 849–863, 1999.
- [9] F. Hyder, I. Kida, K. L. Behar, R. P. Kennan, P. K. Maciejewski, and D. L. Rothman, “Quantitative functional imaging of the brain: Towards mapping neuronal activity by BOLD fMRI,” *NMR Biomed.*, vol. 14, no. 7, pp. 413–431, Nov. 2001.
- [10] R. B. Buxton, K. Uludag, D. J. Dubowitz, and T. T. Liu, “Modeling the hemodynamic response to brain activation,” *NeuroImage*, vol. 23, no. S1, pp. S220–S233, 2004.
- [11] O. Speck, T. Ernst, and L. Chang, “Biexponential modeling of multi-gradient-echo MRI data of the brain,” *Mag. Res. Med.*, vol. 45, no. 6, pp. 1116–1121, Jun. 2001.
- [12] D. A. Yablonskiy, “Quantitation of intrinsic magnetic susceptibility-related effects in a tissue matrix. phantom study,” *Mag. Res. Med.*, vol. 39, no. 3, pp. 417–428, Mar. 1998.
- [13] J. Raz, E. J. Fernandez, and J. Gillespie, “Modeling NMR lineshapes using logspline density functions,” *J. Mag. Res.*, vol. 127, no. 2, pp. 173–183, Aug. 1997.
- [14] O. Speck and J. Hennig, “Functional imaging by  $i_0$  and  $t_2^*$ -parameter mapping using multi-image EPI,” *Mag. Res. Med.*, vol. 40, no. 2, pp. 243–248, Aug. 1998.
- [15] J. P. Wansapura, S. K. Holland, R. S. Dunn, and W. S. Ball, Jr., “NMR relaxation times in the human brain at 3.0 tesla,” *J. Magn. Reson. Imag.*, vol. 9, pp. 531–538, 1999.
- [16] A. M. Howseman, D. L. Thomas, G. S. Pell, S. R. Williams, and R. J. Ordidge, “Rapid  $t_2^*$  mapping using interleaved echo planar imaging,” *Mag. Res. Med.*, vol. 41, no. 2, pp. 368–374, Feb. 1999.
- [17] M. Grüne, F. Pillekamp, W. Schwindt, and M. Hoehn, “Gradient echo time dependence and quantitative parameter maps for somatosensory activation in rats at 7 T,” *Mag. Res. Med.*, vol. 42, no. 1, pp. 118–126, Jul. 1999.
- [18] M. Barth, A. Metzler, M. Klarhöfer, S. Röhl, E. Moser, and D. Leibfritz, “Functional MRI of the human motor cortex using single-shot multiple gradient-echo spiral imaging,” *Mag. Res. Med.*, vol. 17, no. 9, pp. 1239–1243, Nov. 1999.
- [19] A. B. A. Wennerberg, T. Jonsson, H. Forsberg, and T.-Q. Li, “A comparative fMRI study:  $t_2^*$ -weighted imaging versus  $r_2^*$  mapping,” *NMR Biomed.*, vol. 14, no. 1, pp. 41–47, Feb. 2001.
- [20] G. E. Hagberg, M. Bianciardi, F. Patria, and I. Indovina, “Quantitative numart $_2^*$  mapping in functional MRI studies at 1.5 T,” *Mag. Res. Imag.*, vol. 21, no. 10, pp. 1241–1249, Dec. 2003.

- [21] K. P. Pruessmann, M. Weiger, M. B. Scheidegger, and P. Boesiger, "SENSE: Sensitivity encoding for fast MRI," *Magn. Reson. Med.*, vol. 42, pp. 952–962, Nov. 1999.
- [22] M. A. Griswold, P. M. Jakob, R. M. Heidemann, M. Nittka, V. Jellus, J. Wang, B. Kiefer, and A. Haase, "Generalized autocalibrating partially parallel acquisitions (GRAPPA)," *Magn. Reson. Med.*, vol. 47, pp. 1202–1210, 2002.
- [23] A. Maeda, K. Sano, and T. Yokoyama, "Reconstruction by weighted correlation for MRI with time-varying gradients," *IEEE Trans. Med. Imag.*, vol. 7, no. 1, pp. 26–31, Mar. 1988.
- [24] D. C. Noll, C. H. Meyer, J. M. Pauly, D. G. Nishimura, and A. Macovski, "A homogeneity correction method for magnetic resonance imaging with time-varying gradients," *IEEE Trans. Med. Imag.*, vol. 10, no. 4, pp. 629–637, Dec. 1991.
- [25] H. Schomberg, "Off-resonance correction of MR images," *IEEE Trans. Med. Imag.*, vol. 18, no. 6, pp. 481–495, Jun. 1999.
- [26] B. P. Sutton, D. C. Noll, and J. A. Fessler, "Fast, iterative image reconstruction for MRI in the presence of field inhomogeneities," *IEEE Trans. Med. Imag.*, vol. 22, no. 2, pp. 178–188, Feb. 2003.
- [27] J. A. Fessler, S. Lee, V. T. Olafsson, H. R. Shi, and D. C. Noll, "Toeplitz-based iterative image reconstruction for MRI with correction for magnetic field inhomogeneity," *IEEE Trans. Signal Process.*, vol. 53, no. 9, pp. 3393–3402, Sep. 2005.
- [28] E. Schneider and G. Glover, "Rapid *in vivo* proton shimming," *Magn. Res. Med.*, vol. 18, pp. 335–347, Apr. 1991.
- [29] J. A. Fessler, D. Yeo, and D. C. Noll, "Regularized fieldmap estimation in MRI," in *2006 3rd IEEE Int. Symp. Biomed. Imag.: Macro Nano*, Arlington, VA, 2006, pp. 706–709.
- [30] D. C. Noll and W. Schneider, "Theory, simulation, and compensation of physiological motion artifacts in functional MRI," in *Proc. IEEE Int. Conf. Imag.*, Austin, TX, 1994, pp. 40–44.
- [31] D. Raj, A. W. Anderson, and J. C. Gore, "Respiration effects in human functional magnetic resonance imaging due to bulk susceptibility changes," *Phys. Med. Biol.*, vol. 46, no. 12, pp. 3331–3340, 2001.
- [32] X. Hu and S.-G. Kim, "Reduction of signal fluctuation in functional MRI," *Mag. Res. Med.*, vol. 31, pp. 495–503, 1994.
- [33] T. H. Le and X. Hu, "Retrospective estimation and correction of physiological artifacts in fmri by direct extraction of physiological activity from MR data," *Mag. Res. Med.*, vol. 35, no. 3, pp. 290–298, Mar. 1996.
- [34] S. Lee, J. A. Fessler, and D. Noll, "A simultaneous estimation of field inhomogeneity and  $r_2^*$  maps using extended rosette trajectory," in *Proc. Int. Soc. Mag. Res. Med.*, 2002, p. 2327.
- [35] B. P. Sutton, S. J. Peltier, J. A. Fessler, and D. C. Noll, "Simultaneous estimation of  $i_0$ ,  $r_2^*$ , and field map using a multi-echo spiral acquisition," in *Proc. Int. Soc. Mag. Reson. Med.*, 2002, p. 1323.
- [36] D. B. Twieg, "Parsing local signal evolution directly from a single-shot MRI signal: A new approach for fmri," *Mag. Res. Med.*, vol. 50, no. 5, pp. 1043–1052, Nov. 2003.
- [37] V. Roopchansingh, R. W. Cox, A. Jesmanowicz, B. D. Ward, and J. S. Hyde, "Single-shot magnetic field mapping embedded in echo-planar time-course imaging," *Mag. Res. Med.*, vol. 50, no. 4, pp. 839–843, Oct. 2003.
- [38] B. P. Sutton, D. C. Noll, and J. A. Fessler, "Dynamic field map estimation using a spiral-in/spiral-out acquisition," *Mag. Res. Med.*, vol. 51, no. 6, pp. 1194–1204, Jun. 2004.
- [39] D. W. Wilson and B. M. W. Tsui, "Spatial resolution properties of FB and ML-EM reconstruction methods," in *Proc. IEEE Nucl. Sci. Symp. Med. Imag. Conf.*, 1993, vol. 2, pp. 1189–1193.
- [40] J. A. Fessler and W. L. Rogers, "Spatial resolution properties of penalized-likelihood image reconstruction methods: Space-invariant tomographs," *IEEE Trans. Image Process.*, vol. 5, no. 9, pp. 1346–1358, Sep. 1996.
- [41] M. E. Haacke, R. W. Brown, M. R. Thompson, and R. Vankatesan, *Magnetic Resonance Imaging, Physical Principles and Sequence Design*. New York: Wiley, 1999.
- [42] M. Hestenes and E. Stiefel, "Methods of conjugate gradients for solving linear systems," *J. Res. Nat. Bureau Standard*, vol. 49, pp. 409–436, 1952.
- [43] J. A. Fessler and B. P. Sutton, "Nonuniform fast fourier transforms using min-max interpolation," *IEEE Trans. Signal Process.*, vol. 51, no. 2, pp. 560–574, Feb. 2003.
- [44] V. Olafsson, D. C. Noll, and J. A. Fessler, "Spatial resolution analysis of iterative image reconstruction with separate regularization of real and imaginary parts," in *Proc. 3rd IEEE Int. Symp. Biomed. Imag.: Macro Nano*, Arlington, VA, 2006, pp. 5–8.
- [45] M. S. Cohen, "Parametric analysis of fMRI data using linear systems methods," *NeuroImage*, vol. 6, no. 2, pp. 93–103, Aug. 1997.
- [46] S. D. Forman, J. D. Cohen, M. Fitzgerald, W. F. Eddy, M. A. Mintun, and D. C. Noll, "Improved assessment of significant activation in functional magnetic resonance imaging (fMRI): Use of a cluster-size threshold," *Mag. Res. Med.*, vol. 33, no. 5, pp. 636–647, May 1995.
- [47] J. A. Fessler and D. C. Noll, "Model-based MR image reconstruction with compensation for through-plane field inhomogeneity," in *Proc. IEEE Int. Symp. Biomed. Imag.*, Apr. 2007, pp. 920–923.
- [48] D. C. Noll, C. R. Genovese, L. E. Nyström, A. L. Vazquez, S. D. Forman, W. F. Eddy, and J. D. Cohen, "Estimating test-retest reliability in functional MR imaging, ii: Application to motor and cognitive activation studies," *Mag. Res. Med.*, vol. 38, no. 3, pp. 508–517, Sep. 1997.
- [49] T. Hastie, R. Tibshirani, and J. H. Friedman, *The Elements of Statistical Learning*. New York: Springer Verlag, 2001.
- [50] V. Olafsson, J. A. Fessler, and D. C. Noll, "Dynamic updates of  $r_2^*$  and field map in fMRI using a spiral-in quick-spiral-out k-space trajectory," in *Proc. Int. Soc. Mag. Reson. Med.*, 2006, p. 2838.